



Deposited via The University of Sheffield.

White Rose Research Online URL for this paper:

<https://eprints.whiterose.ac.uk/id/eprint/147235/>

Version: Accepted Version

Article:

Cepero-Mejías, F., Curiel-Sosa, J.L., Zhang, C. et al. (2019) Effect of cutter geometry on machining induced damage in orthogonal cutting of UD polymer composites: FE study. *Composite Structures*, 214. pp. 439-450. ISSN: 0263-8223

<https://doi.org/10.1016/j.compstruct.2019.02.012>

Article available under the terms of the CC-BY-NC-ND licence
(<https://creativecommons.org/licenses/by-nc-nd/4.0/>).

Reuse

This article is distributed under the terms of the Creative Commons Attribution-NonCommercial-NoDerivs (CC BY-NC-ND) licence. This licence only allows you to download this work and share it with others as long as you credit the authors, but you can't change the article in any way or use it commercially. More information and the full terms of the licence here: <https://creativecommons.org/licenses/>

Takedown

If you consider content in White Rose Research Online to be in breach of UK law, please notify us by emailing eprints@whiterose.ac.uk including the URL of the record and the reason for the withdrawal request.

Effect of cutter geometry on machining induced damage in orthogonal cutting of UD polymer composites: FE study

Cepero-Mejías F.^{a,b,c,*}, Curiel-Sosa J. L.^{b,c}, Zhang C.^d, Phadnis V. A.^e

^a*Industrial Doctorate Centre in Machining Science, The University of Sheffield, Sir Frederick Mappin Building, Mappin Street, S1 3JD Sheffield, United Kingdom.*

^b*Computer-Aided Aerospace & Mechanical Engineering (CA2M) Research Group, Sir Frederick Mappin Building, Mappin Street, S1 3JD Sheffield, United Kingdom.*

^c*Department of Mechanical Engineering, The University of Sheffield, Sir Frederick Mappin Building, Mappin Street, S1 3JD Sheffield, United Kingdom.*

^d*School of Mechanical Engineering, Jiangsu University, Zhenjiang, China*

^e*AMRC with Boeing, Advanced Manufacturing Park, Wallis Way, Catcliff, Rotherham, S605TZ, United Kingdom.*

Abstract

This article presents a finite-element analysis (FEA) based study to understand the influence of cutting parameters (rake angle, relief angle and cutter edge radius) on the machining-induced damage of unidirectional (UD) composites. Carbon/epoxy (CFRP) and glass/epoxy (GFRP) composites are considered. Onset of damage in composites is modelled using a combination of maximum stress and Puck's fracture criteria, while a novel damage propagation algorithm is proposed to account for the post-damage material softening behaviour. A spring-back phenomenon (partial elastic recovery of workpiece material after tool passed a cutting surface) often observed in composites machining, is considered in the FE model to allow a better prediction of the thrust force and induced damage. A validated FE model predicts that with increasing relief angle, the extent of sub-surface damage is reduced. Rake angle or tool edge radius are not found to have a great influence on the induced damage. A large dependence is observed between the fibre angle and the induced damage, as the severity of damage increase when fibre orientations varies from 30° to 90°.

Keywords: Machining, Induced machining damage, Finite element, Modelling, Orthogonal cutting, Composite

1. Introduction

In the last decade, the use of polymer matrix composites (PMCs) has become widespread due to their superior properties. PMCs are often manufactured to a near-net shape, though require finish

*Corresponding author.

Email addresses: fmcepero1@sheffield.ac.uk (Cepero-Mejías F.), j.curiel-sosa@sheffield.ac.uk (Curiel-Sosa J. L.), zhangchao@ujs.edu.cn (Zhang C.), v.phadnis@sheffield.ac.uk (Phadnis V. A.)

URL: <https://www.ms-idc.co.uk/meet-students> (Cepero-Mejías F.), <https://www.sheffield.ac.uk/mecheng/staff/jcurielsosa> (Curiel-Sosa J. L.)

Preprint submitted to Composite Structures

January 31, 2019

4 cutting operations to remove excess material and achieve strict assembly tolerances. Machining
5 PMCs is typically challenging owing to intrinsic properties of its constituents. During machining,
6 tougher polymer resins and hard fibres could cause excessive mechanical stress on the cutting
7 edge, while low thermal conductivity of resins bypasses the majority of process heat to a cutting
8 tool, resulting in accelerated wear. Consequently, blunt cutting tools with unfavourable cutting
9 parameters bend fibres ahead of the cutting tool tip rather than shearing them away [1, 2]. This
10 thermo-mechanical abuse gives rise to a variety of damage modes in PMCs such as fibre/resin
11 pull-out, resin thermal-degradation and delamination [3–5]. The resultant damage sites, in turn,
12 could affect the surface quality of a machined component and act as potential crack nucleation
13 sites when loaded in service [6].

14 A large number of cutting trials are generally needed to fully characterise machining responses
15 (typically, cutting forces, cut surface quality, surface and sub-surface damage and tool wear) of
16 a particular combination of a fibre/matrix system and cutting tool geometry. This could be a
17 cumbersome and very costly venture. Numerical models of machining accounting for appropriate
18 material constitutional relationships, underlying physics and validated using experimental data can
19 be a great virtual alternative in such cases.

20 Analytical models predicting composites machining responses are primarily limited to calcula-
21 tions of critical force responsible for delamination initiation in drilling applications [7], and tool
22 wear on the simplified tool geometries. Several underpinning complexities such as heterogene-
23 ity of thermo-mechanical properties of PMCs, complex cutter geometries and dynamic friction
24 changes in high-speed machining, as well as high strain rate-effects limit the use of analytical
25 models. FE models on the other hand, though, are not computationally as economical, pose a
26 viable option to study all above mentioned parameters in depth.

27 Various length-scale approaches (micro-, meso- and macro-scale) are used to model machining
28 response of composites depending upon the motivation of the study. For example, micro-scale FE
29 models simulating orthogonal cutting of composites [8–12] allow prediction of machining damage

30 to individual fibre/matrix constituents as well as fibre-matrix de-bonding. These computational
31 analyses can provide fairly accurate information on localised damage, though are complex and
32 computationally expensive for the amount of the information that can be extracted. Macro-scale
33 FE models, on the other hand, consider use of homogenised material properties. A variety of
34 fibre/matrix damage modes and their interactions can be simulated using advanced mathematical
35 criteria accounting for fracture and damage mechanics [13–15]. Cohesive zone modelling (CZM)
36 approach is also popular amongst researchers to model interply delamination [16].

37 A limited number of studies incorporating a full 3D FE model of composite machining are
38 available to date, and mostly focussed at predicting interply delamination in orthogonal cutting
39 application [17–20], mainly due to the extent of computational resources needed. Consequently,
40 majority of published FE models consider 2D plane stress approximation [21–28] to analyse influ-
41 ence of cutting parameters on the subsurface damage. Few interesting studies and their outcomes
42 are briefed next. Santiuste et al. [21] developed a 2D FE model of orthogonal cutting to demon-
43 strate that the subsurface damage was much reduced in machining brittle (CFRP) composites than
44 in ductile (GFRP) composites. They further developed a 3D model of the same process accounting
45 for thermal effects [29] the model though accounts for cutting force prediction and chip formation
46 successfully, fails to consider interaction of thermal degradation of resin properties and the overall
47 workpiece stiffness reduction due to mechanical damage. In another study aimed at understanding
48 influence of cutting parameters on the machining response of composites, Zenia et al. [22] iden-
49 tified fibre orientation, rake angle and depth of cut as critical factors affecting cutting forces and
50 induced damage. It was suggested that increase in the depth of cut could lead to higher cutting
51 forces and induced damage, while increase in rake angle reduce the same. Soldani et al. [23] also
52 considered the effect of cutting edge radius along with other cutter geometry parameters, and con-
53 cluded that the use of a sharper tool edge radius can reduce the subsurface damage significantly.
54 A critical review of these state-of-the-art FE models suggests that though these could be used to
55 predict machining response terms of induced damage, chip morphology, and cutting forces; data

56 used in their validation is often very limited. For example, most of the published FE models
57 studying composites machining are validated by comparing numerically predicted cutting forces
58 with the experimental data [30–32], though an extent of machining induced damage is usually not
59 measured for a validation purpose.

60 In the current work, a 2D FE model of orthogonal cutting of UD CFRP composite is presented.
61 It accounts for the effect of various cutting parameters - cutter rake and relief angle, cutting edge
62 radius and fibre orientation- on machining induced damage of composites. FE model employ a
63 combination of maximum stress and Pucks fracture criteria to model damage initiation based on
64 critical stress value, while post-damage material softening is accounted for using an energy-based
65 approach. Mechanics for material spring-back is also considered. FE models are validated using
66 experimental cutting force data as well as optical measurements of machining induced damage
67 [24].

68 **2. Model characteristics**

69 Several 2D FEM plane stress quasi-static analysis are performed with the numerical software
70 package Abaqus/Explicit. Positive fibre orientations of 0° , 15° , 30° , 45° , 60° , 75° and 90° are as-
71 sessed in this work. A standard cutting configuration coherent with parameters used for Bhatnagar
72 et al. [24] in their experiments is considered to validate the numerical results. Fig. 1 shows an
73 schematic illustration of cutting parameters treated ahead.

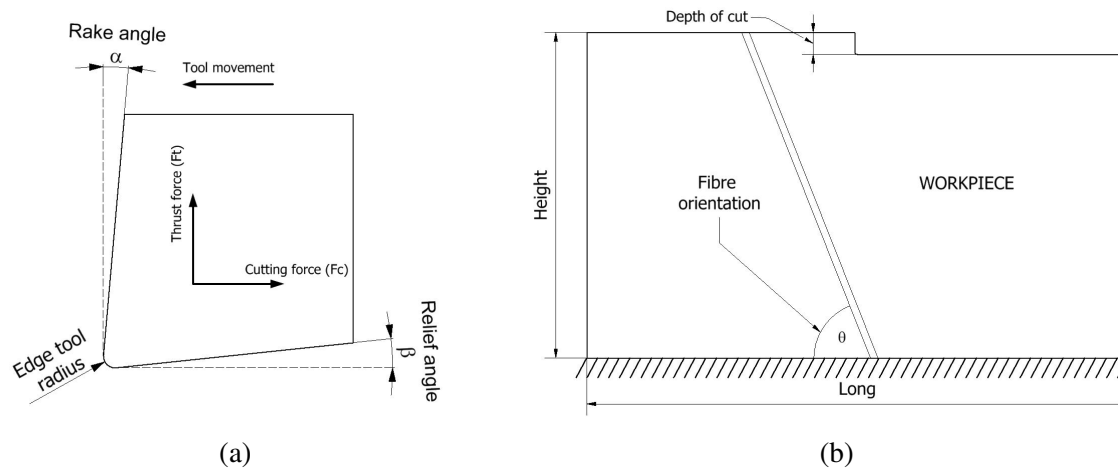


Fig. 1. (a) Tool and (b) workpiece cutting parameters.

74 **2.1. Machining configurations and geometric analysis**

75 To evaluate the induced damage influence of rake angle, relief angles, tool edge radius and
 76 workpiece material ten cutting configurations are simulated. The desired cutting variable studied
 77 is changed to keep the rest of cutting variables the same values with the standard configuration. In
 78 Table 1 a representation of all cutting variables values examined in this work is offered.

Table 1

Cutting variables employed in this work

| Cutting variables | Standard configuration | Cutting variables values studied |
|------------------------------------|------------------------|----------------------------------|
| Rake angle (α) | 5° | -5°, 0°, 10° |
| Relief angle (β) | 6° | 4°, 8°, 10° |
| Tool edge radius (μm) | 50 | 30, 15 |
| Depth of cut (mm) | 0.2 | - |
| Workpiece material | GFRP | CFRP |
| Cutting speed (mm/s) | 8.33 | - |

79 A 5 mm long and 3 mm height workpiece are investigated. As a boundary condition, workpiece
 80 bottom side is fixed while for lateral sides the horizontal displacement is restricted as shown in
 81 Fig. 2. Elastic and strength properties of UD-GFRP and UD-CFRP used in this work are extracted
 82 from the Santiuste et al. [21] and Phadnis et al. [16] publications, respectively. Table 2 and Table 3
 83 collects the elastic and strength properties of the studied UD-GFRP and UD-CFRP composites.

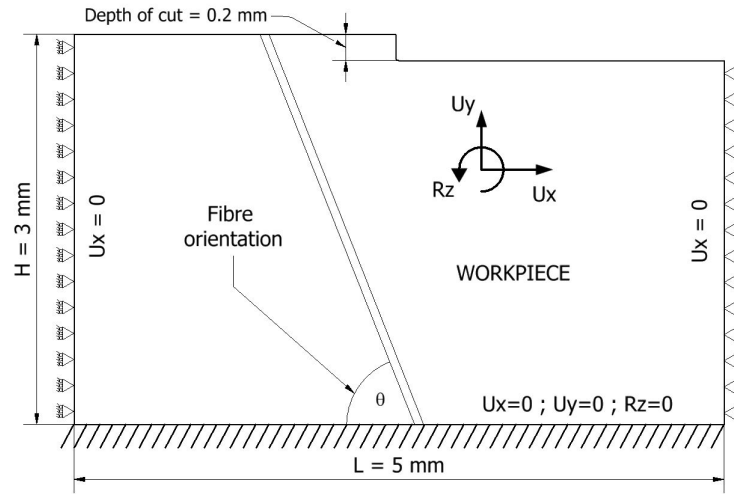


Fig. 2. Workpiece boundary conditions.

Table 2

Elastic properties of GFRP and CFRP materials used in this work

| Material | $E_{11}(GPa)$ | $E_{22}(GPa)$ | $G_{12}(GPa)$ | ν_{12} |
|-----------|---------------|---------------|---------------|------------|
| GFRP [21] | 48 | 12 | 6 | 0.28 |
| CFRP [16] | 136.6 | 9.6 | 5.2 | 0.29 |

Table 3

Strength properties of GFRP and CFRP materials used in this work

| Material | $X_T(MPa)$ | $X_C(MPa)$ | $Y_T(MPa)$ | $Y_C(MPa)$ | $S(MPa)$ |
|-----------|------------|------------|------------|------------|----------|
| GFRP [21] | 1200 | 800 | 59 | 128 | 25 |
| CFRP [16] | 2720 | 1690 | 111 | 214 | 115 |

84 **2.2. Meshing parameters**

85 Quadrilateral elements with linear interpolation and reduced integration (CPS4R) are selected.
 86 Deletion of elements is not considered in this work. Besides, the low cutting speed applied in
 87 the simulation make the FEM analysis could be considered as a quasi-static problem. This issue
 88 allows increasing the composite density while the model kinematic energy stands in low values
 89 without affecting the final results. In this model, density is increased using an appropriate mass
 90 scaling factor until achieving an integration time of around 10^{-8} and 10^{-9} s.

91 Mesh element size is selected to reach a right time-accuracy combination. A rectangular zone
92 next to the cutting tool meshed with a medium element size of $10\ \mu m$. The remaining area is more
93 coarsely mesh using partitions which increase the element size progressively from the $10\ \mu m$ in
94 the refined mesh vicinity until achieving the value of $100\ \mu m$ in the outer edges. These partitions
95 avoid the excessive element distortion and improve the numerical results quality (refer to Fig. 3).

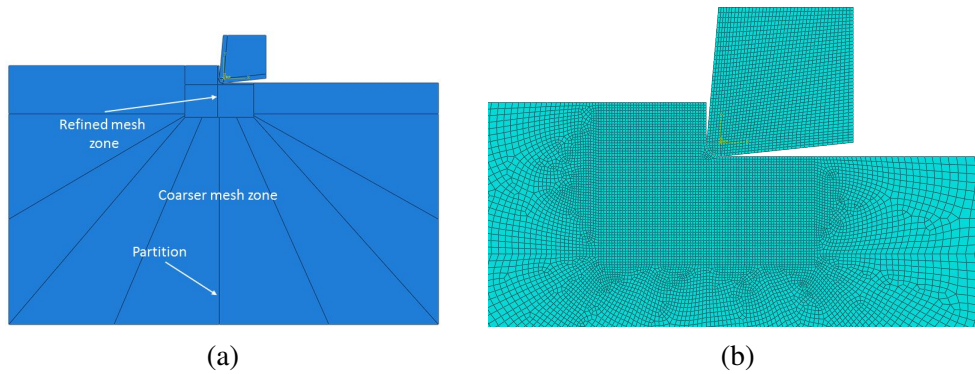


Fig. 3. (a) Mesh distribution and (b) Zoom of the refined mesh area.

96 2.3. Contact and friction modelling

97 The tool is considered as a solid rigid body. The contact between the tool and the workpiece is
98 performed with a surface-node surface contact property. A constant Coulomb friction coefficient
99 of 0.2 is employed in all simulations. This is not the best method to model the contact, because
100 the friction coefficient should vary with the fibre orientation. However, because of the lack of
101 information in this matter, other authors have been using this methodology for simulating the
102 tool-workpiece friction [21, 22, 25].

103 3. FEM damage algorithm basics

104 The new proposed damage algorithm was implemented in Abaqus/explicit through a user sub-
105 routine VUMAT. Constitutive equations considered in this work are extracted from the damage
106 model proposed by Lapczyk and Hurtado [33]. In this formulation, four different damage modes

107 are present: fibre traction (d_{ft}), fibre compression (d_{fc}), matrix traction (d_{mt}) and matrix compres-
 108 sion (d_{mc}). Hereafter, the combination of these damage modes inside stiffness matrix is showcased
 109 in Eq. (1).

$$\begin{bmatrix} \sigma_{11} \\ \sigma_{22} \\ \sigma_{12} \end{bmatrix} = \begin{bmatrix} (1 - d_f)E_{11} & (1 - d_f)(1 - d_m)v_{21}E_{11} & 0 \\ (1 - d_f)(1 - d_m)v_{12}E_{22} & (1 - d_m)E_{22} & 0 \\ 0 & 0 & (1 - d_s)G_{12} \end{bmatrix} \begin{bmatrix} \varepsilon_{11} \\ \varepsilon_{22} \\ \varepsilon_{12} \end{bmatrix} \quad (1)$$

, where $D = 1 - (1 - d_f)(1 - d_m)v_{12}v_{21}$; $d_s = 1 - (1 - d_{ft})(1 - d_{fc})(1 - d_{mt})(1 - d_{mc})$

$d_f = \max\{d_{ft}, d_{fc}\}$; $d_m = \max\{d_{mt}, d_{mc}\}$; $d_I \in [0, 1]$ and $I = (ft, fc, mt, mc)$

110 Because of composite brittle behaviour matrix plasticity is not taken into account. In addition,
 111 isothermal conditions are contemplated in this work for simplicity. Composites material behaviour
 112 is modelled with an initial linear elastic response until damage initiation took place. The maximum
 113 stress failure criterion is selected to determine the fibre damage initiation, while for the matrix the
 114 Puck plane stress failure criterion is chosen. Five distinct damage modes are considered, fibre
 115 traction, fibre compression, matrix mode A, matrix mode B and matrix mode C.

116 Equations to reach the fibre traction and fibre compression damage initiation criteria are repre-
 117 sented in Eqs. (2) and (3).

- 118 • Fibre traction ($\sigma_{11} > 0$)

$$F_{ft} = \left(\frac{\sigma_{11}}{X_T} \right) \geq 1 \quad (2)$$

- 119 • Fibre compression ($\sigma_{11} < 0$)

$$F_{fc} = \left| \frac{\sigma_{11}}{X_C} \right| \geq 1 \quad (3)$$

120 Where F_{ft} and F_{fc} represents the fibre traction and compression damage activation functions,
 121 respectively. Henceforth, these damage activation functions are named only activation functions
 122 for simplicity. Plane stress failure Puck criteria modes are chosen because it offers good matrix

123 failure predictions in comparison with other extended composites failure criteria [34]. In this
 124 document, the basics of this failure are provided. For completion, a brief explanation of the Puck
 125 matrix failure modes variables is given. Interested reader is referred to [35] for a more detailed
 126 information.

127 Matrix plane stress Puck failure criteria are composed of three failure modes: (1) Mode A, (2)
 128 Mode B and (3) Mode C. In Mode A matrix rupture is occasioned under traction conditions, while
 129 Mode B and Mode C are taken place under normal compressive stresses. Mode A and Mode B
 130 cut the laminate in parallel with thickness direction while Mode C split the laminate with a certain
 131 angle. Puck matrix failure modes predictions contain a high level of complexity as appreciated in
 132 Eqs. (4) to (6).

133 F_{mma} , F_{mmb} and F_{mmc} represents the Mode A, Mode B and Mode C damage activation functions,
 134 respectively. To clarify the analysis of results only a matrix traction activation function (F_{mt}) and
 135 matrix compression activation function (F_{mc}) are analysed. Value of (F_{mt}) is assigned to be the
 136 same than F_{mma} , while (F_{mc}) is established as the maximum of F_{mmb} and F_{mmc} in every element
 137 ($F_{mc} = \max\{F_{mmb}, F_{mmc}\}$).

138 **Matrix traction activation function ($F_{mt} = F_{mma}$)**

- 139 • Matrix Mode A ($\sigma_{22} \geq 0$)

$$F_{mma} = \sqrt{\left(\frac{\sigma_{12}}{R_{\perp\parallel}^A}\right)^2 + \left(1 - \frac{p_{\perp\parallel}^{(+)}}{R_{\perp\parallel}^A} R_{\perp}^{(+A)}\right)^2 \left(\frac{\sigma_{22}}{R_{\perp}^{(+A)}}\right)^2} + \frac{p_{\perp\parallel}^{(+)}}{R_{\perp\parallel}^A} \sigma_{22} \geq 1 \quad (4)$$

140 **Matrix compression activation function ($F_{mc} = \max\{F_{mmb}, F_{mmc}\}$)**

- 141 • Matrix Mode B ($\sigma_{22} < 0$ and $\sigma_{22} > -R_{\perp\perp}^A$)

$$F_{mmb} = \sqrt{\left(\frac{\sigma_{12}}{R_{\perp\parallel}^A}\right)^2 + \left(\frac{p}{R}\right)^2 \sigma_{22}^2} + \left(\frac{p}{R}\right) \sigma_{22} \geq 1 \quad (5)$$

142

- Matrix Mode C ($\sigma_{22} \leq -R_{\perp\perp}^A$)

$$F_{mmc} = \frac{1}{2 \left[1 + \left(\frac{p}{R} \right) R_{\perp\perp}^A \right]} \left[\left(\frac{\sigma_{12}}{R_{\perp\parallel}^A} \right)^2 + \left(\frac{\sigma_{22}}{R_{\perp\perp}^A} \right)^2 \right] \frac{R_{\perp\perp}^A}{-\sigma_{22}} \geq 1 \quad (6)$$

143

Here, all terms with R represent the strength components associated with the fracture plane.

144

Term $R_{\perp\parallel}^{(+A)}$ is equal to the transverse matrix traction strength (Y_T), $R_{\perp\parallel}^A$ corresponds to the intralam-

145

inar shear strength (S_{12}). Variable $R_{\perp\perp}^A$ is the transverse/transverse shear strength and generally

146

this variable is quite difficult to measure, so the value is normally extracted indirectly from Eq. (7).

147

Term $p_{\perp\parallel}^{(+)}$ is the Puck failure envelope slope when $\sigma_{22} > 0$ at point $\sigma_{22} = 0$. Recommendable val-

148

ues for this variable are 0.35 for carbon fibre composites and 0.3 for glass fibre composites [36].

149

Expression $\left(\frac{p}{R} \right)$ is calculated using the equation formulated in Eq. (8).

$$R_{\perp\perp}^A = \frac{Y_C}{2 \left(1 + p_{\perp\perp}^{(-)} \right)} \quad (7)$$

$$\left(\frac{p}{R} \right) = \frac{p_{\perp\parallel}^{(-)}}{R_{\perp\parallel}^A} \quad (8)$$

150

In the above equations, values recommended for the variables $p_{\perp\perp}^{(-)}$ and $p_{\perp\parallel}^{(-)}$ are 0.3 for carbon

151

fibre composites and 0.25 for glass fibre composites [36].

152

After damage onset is achieved, a linear continuum damage mechanics (CDM) approach is

153

performed. The expression used to calculate the damage modes quantity in every step is shown in

154

Eq. (9).

$$d_I = \frac{\delta_{I,eq}^f \left(\delta_{I,eq} - \delta_{I,eq}^0 \right)}{\delta_{I,eq}^f \left(\delta_{I,eq}^f - \delta_{I,eq}^0 \right)} \quad (d_I \in [0, 1] \text{ and } I = (ft, fc, mt, mc)) \quad (9)$$

155

Final ($\delta_{I,eq}^f$) and initial ($\delta_{I,eq}^0$) equivalent displacements are calculated immediately after the dam-

156

age initiation condition of one damage mode is reached. These terms are determined by Eq. (10)

157

and Eq. (11), respectively. Fracture toughness values show in Table 4 are employed in the present

158

work.

Table 4

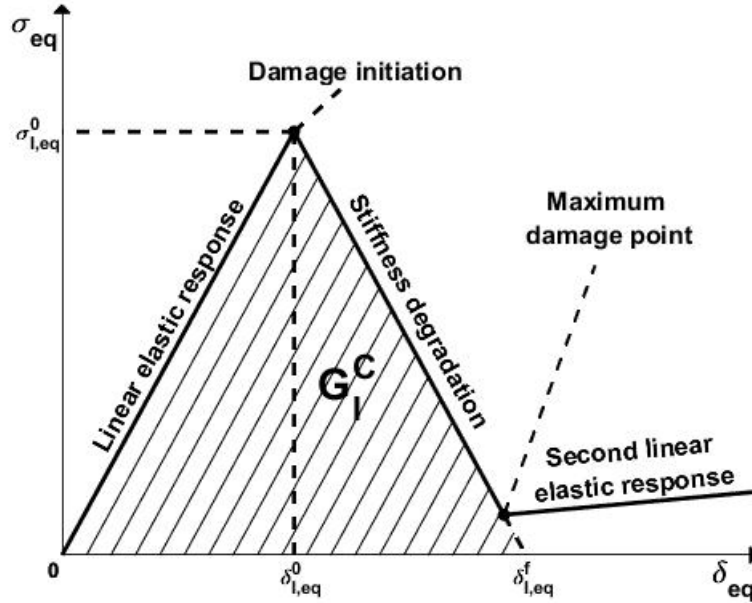
Critical fracture toughness extracted from [37]

| N/mm | G_{ft}^c | G_{fc}^c | G_{mt}^c | G_{mc}^c |
|-----------------------------|------------|------------|------------|------------|
| Critical fracture toughness | 10 | 10 | 1 | 1 |

$$\delta_{I,eq}^f = \frac{2G_I^c F_I}{\sigma_{I,eq}} \quad (10)$$

$$\delta_{I,eq}^0 = \frac{\delta_{I,eq}}{F_I} \quad (11)$$

159 In the above equations, coefficient F_I with $I = (ft, fc, mt, mc)$ represents the activation function
 160 value of the correspondent damage mode. $\sigma_{I,eq}$ and $\delta_{I,eq}$ are the equivalent stress and displacements
 161 of a damage mode, respectively. Expressions assigned to obtain the value of these variables are
 162 explained in detail in Ref. [33].

**Fig. 4.** Damage model scheme carried out for every damage mode.

163 Finally, maximum damage of 0.95 is allowed for the matrix and 0.999 for the fibre damage
 164 modes. These maximum values are chosen to avoid numerical errors [25] and simulate the re-
 165 maining stiffness that a total failure ply supply to adjacent laminate plies [36]. After this damage

166 level was achieved a second linear elastic response is introduced with the remaining stiffness. An
167 illustration of the material behaviour scheme carried out is represented in Fig. 4.

168 **4. Model validation**

169 The standard cutting configuration model is validated by comparison with the experimental
170 results obtained by Bhatnagar et al. [24]. The chip is assumed to be formed when the simulated
171 cutting force reaches the experimental values obtained. Cutting and thrust forces are registered
172 until the chip formation process was accomplished. Maximum cutting and thrust forces simulated
173 are chosen as the machining forces to analyse the numerical results.

174 This assumption is considered reasonable, because of the non-deletion of elements carried out in
175 the simulations avoid the apparition of the natural machining forces fluctuations [25]. An example
176 of one simulation records of the cutting and thrust forces is provided in Fig. 5.

177 Spring back phenomenon, which consider the partial laminate thickness recovery that always
178 takes place after the tool pass away (Fig. 5), is taken to improve the numerical damage predictions.
179 This concept is introduced, imposing a linear progressive vertical penetration to the tool, while it
180 is advancing horizontally; final vertical displacements for every fibre orientations are chosen in
181 the order of the half or one tool edge radius value as studied by Wang et al. [38] and they are
182 showcased in Table 5. This approach is developed to avoid the excessive meshed elements distor-
183 tion under the tool that take place when only vertical displacement is applied. The real depth of
184 cut considered is 0.2 mm, while to calculate the nominal depth of cut the vertical tool penetration
185 should be added, see Table 5.

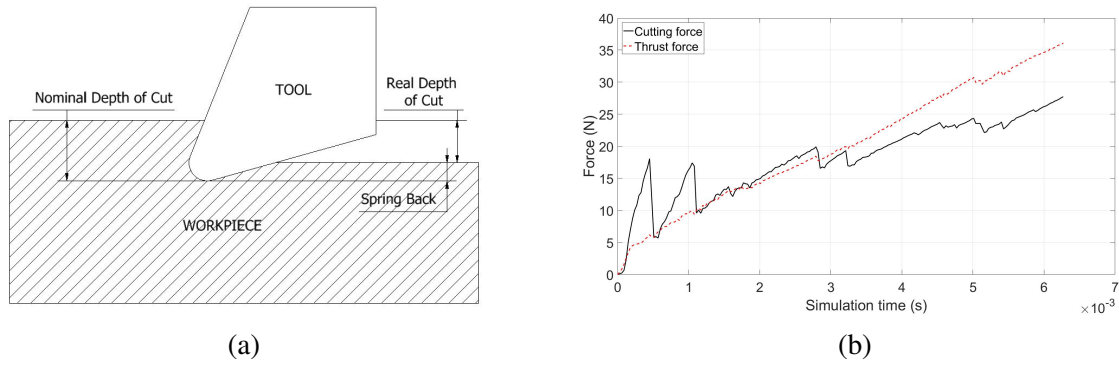


Fig. 5. (a) Spring back phenomenon representation and (b) example of machining forces record for the simulation of the standard cutting configuration and a fibre orientation of 0° .

186 Lasri et al. [25] and Santiuste et al. [21] validated their simulations using the cutting force
 187 obtained in Bhatnagar et al. [24] experiments. However, thrust force is poorly predicted as a result
 188 of not including the spring back phenomenon effects on composite machining response. This
 189 work proves the importance of this phenomenon on thrust force enhancing previous numerical
 190 predictions, as shown in Fig. 5.

191 In addition, the machining sub-surface damage is assessed through the activation functions
 192 (F_{ft} , F_{fc} , F_{mt} and F_{mc}) introduced previously. Sub-surface damage is assumed to be the verti-
 193 cal distance between the lowest element where it is equalised or exceeded the damage initiation
 194 condition and the machining trim surface. In this work the damage initiation condition is achieved
 195 after reaching or exceed F_{mt} and F_{fc} a value of 0.75 or F_{mc} and F_{ft} a value of 1. This decision is
 196 taken because fibre experience buckling problems in compression states and matrix have proper-
 197 ties degradation problems in traction states [36]. Therefore, it is decided to be conservative with
 198 fibre compression and matrix traction damage modes.

Table 5

Vertical speed, cutting tool displacements and simulation time obtained for every fibre orientation simulating the standard cutting configuration

| Fibre orientation | 0° | 15° | 30° | 45° | 60° | 75° | 90° |
|------------------------------|-----------|------------|------------|------------|------------|------------|------------|
| Vertical penetration (mm) | 0.0313 | 0.0226 | 0.0411 | 0.0395 | 0.0407 | 0.0439 | 0.0600 |
| Nominal depth of cut (mm) | 0.2313 | 0.2226 | 0.2411 | 0.2395 | 0.2407 | 0.2439 | 0.2600 |
| Horizontal displacement (mm) | 0.0521 | 0.0236 | 0.0381 | 0.0366 | 0.0679 | 0.1465 | 0.3202 |
| Simulation time (s) | 0.0063 | 0.0029 | 0.0046 | 0.0044 | 0.0082 | 0.0176 | 0.0394 |

199 From the results is obtained that fibre damage initiation criterion is not reached in low laminate
 200 locations. Hence, the matrix damage modes determine the sub-surface damage in all simulations.
 201 In Fig. 7 the evolution of matrix damage modes and shear and transverse stresses in different lam-
 202 inate areas is assessed, see Fig. 7. Three distinct matrix induced damage modes are distinguished
 203 in different workpiece positions: (1) beneath, (2) behind and (3) in front of the tool.

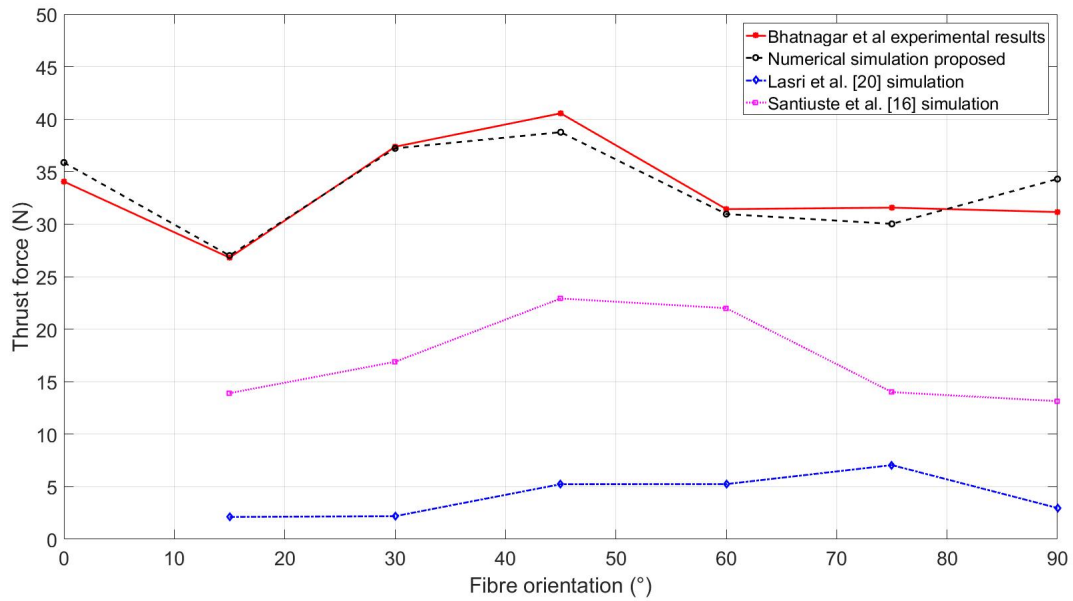


Fig. 6. Thrust forces obtained in the proposed numerical simulation and other publications.

204 As shown in Fig. 7(d), d_{mt} is found behind, while d_{mc} occurs in front positions as illustrated
 205 in Fig. 7(e). Both matrix damage modes are obtained in low laminate positions (Fig. 7(c)). For
 206 clarification, failure allocations in Puck's failure envelope is provided in Fig. 7(f). Main reasons
 207 to obtain these results are:

- 208 • Zone 1: Shear stresses are predominant, allocating the failure point in the boundary be-
 209 tween traction and compression failure modes.
- 210 • Zone 2: Important traction transverse stresses are obtained because the pulling effect of
 211 the tool tip produce a Mode A or matrix traction failure.

- 212 • Zone 3: Mode C or matrix compression damage is detected due to the high compressive
 213 transverse stresses produced by the pushing action of the tool.

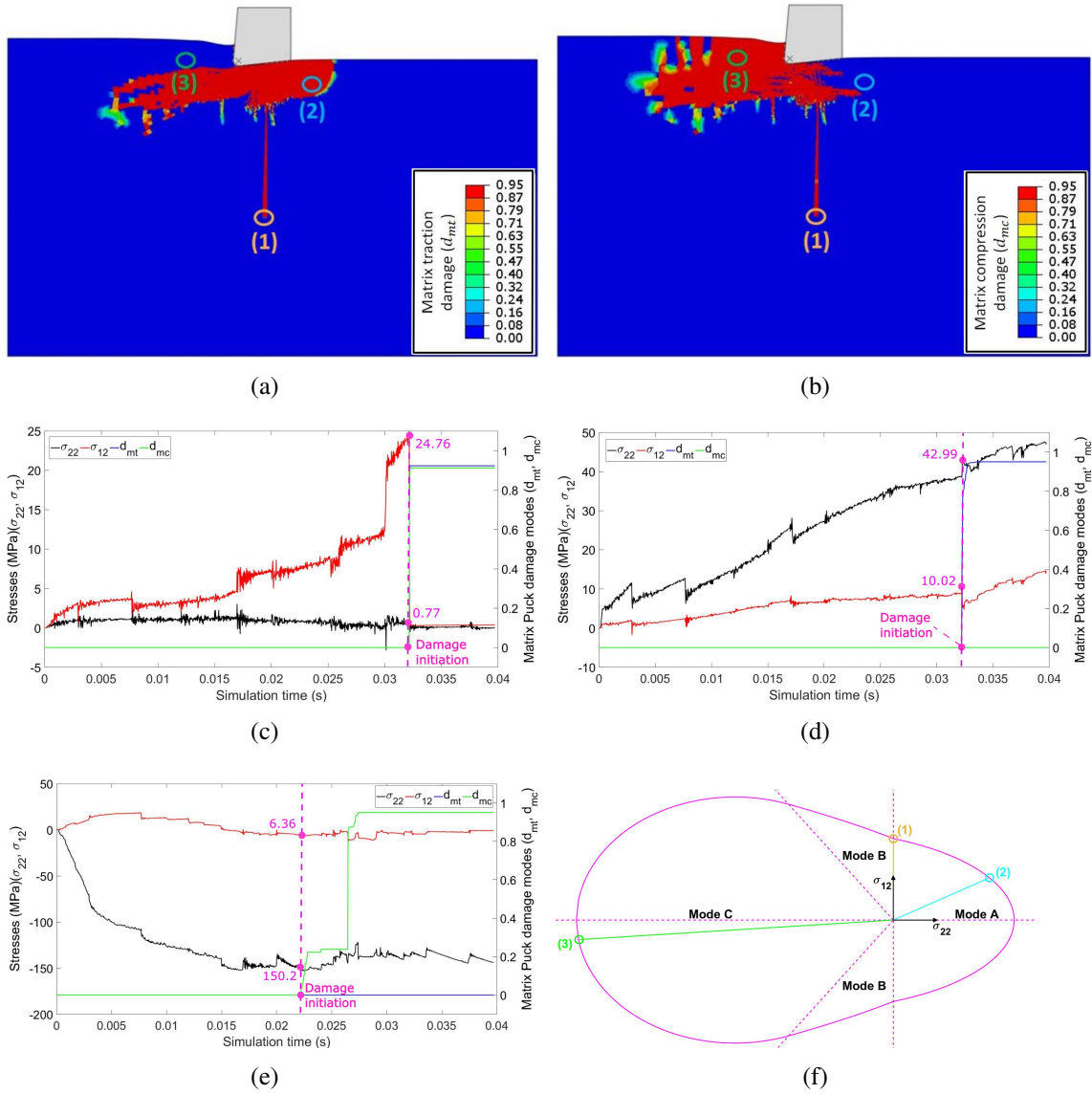


Fig. 7. Detailed illustrations of the matrix damage modes causes at final simulation time with the standard configuration and a fibre orientation of 90° : (a) Matrix traction damage (d_{mt}), (b) Matrix compression damage d_{mc} , (c), (d), (e) σ_{22} , σ_{12} , d_{mt} and d_{mc} predicted in position (1), (2) and (3), respectively and (f) Damage modes allocation using the Puck's matrix failure criterion in different laminate positions

214 Finally, the maximum sub-surface damage measured in the simulations achieved a significant
 215 improvement in comparison with Bhatnagar et al. [24] results, as depicted in Fig. 8. For all fibre

216 orientations excepting 90° the predicted values are closer to experimental ones than the Bhatna-
217 gar's predictions achieved.

218 This fact could be solved with the inclusion of matrix plastic deformation; it would increase
219 the energy required to move the tool and increment the sub-surface damage predictions. Besides,
220 the fibre/matrix debonding has a relevant role for high fibre orientations 60-90°; this fibre bending
221 effect would increase appreciably the predicted damage depth, especially for a fibre orientation of
222 90°. This factor is not included in this work, the development of a micro mechanical FE model
223 should be required to analyse these particular cases to obtain more accurate predictions. However,
224 the influence of cutter geometries on the induced damage is still affordable with this numerical
225 model as both numerical and experimental results follow the same trend.

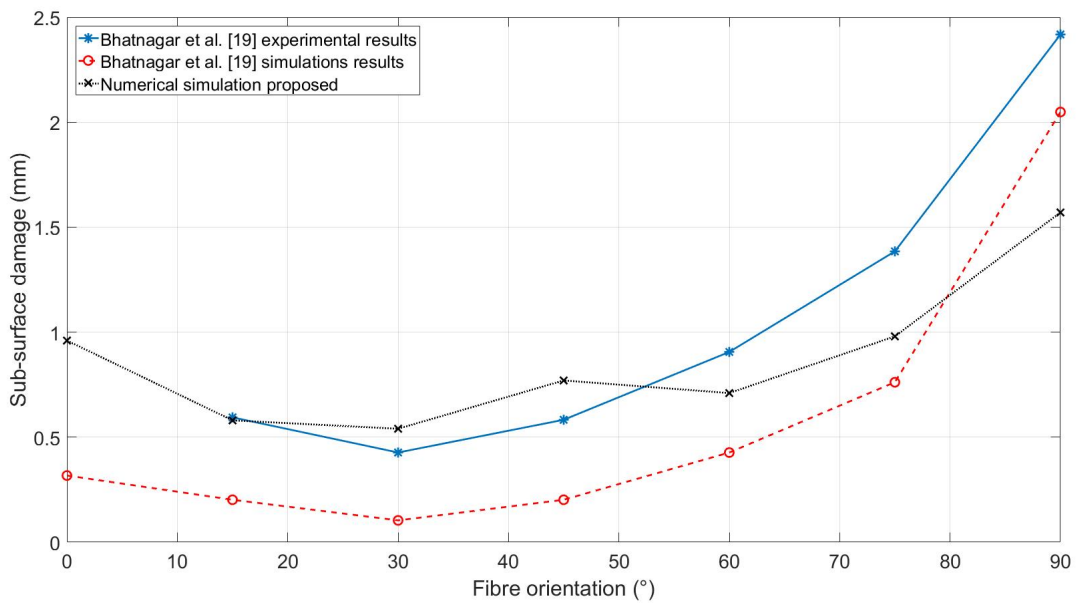


Fig. 8. Sub-surface damage obtained in the numerical simulation proposed and Bhatnagar et al. [24] numerical and experimental results

226 5. Results and discussion

227 Main contributions in this article are summarized in this section. For all simulations performed
228 only one of the desired cutting parameters is changed, keeping the rest with the standard config-

229 uration values (refer to Table 1). In order to compare the influence of cutting parameters on the
230 induced machining damage, ten cutting configurations are assessed. They are performed apply-
231 ing the same tool displacement and velocities used for the standard cutting configuration (refer to
232 Table 5).

233 5.1. Fibre orientation influence

234 In this work, the damage activation function is used to reflect the predicted sub-surface dam-
235 age area accounting the initial damage conditions exposed in section 3 ($F_{mt} = 1$ or $F_{mc} \geq 0.75$).
236 Therefore, these variables not only point the damage areas, but also indicate the laminate zones
237 where damage is close to occur and residual stresses might be found. Henceforth, for brevity pur-
238 pose, only F_{mt} or F_{mc} will be shown in every section as both functions predicts similar sub-surface
239 damages below the tool, as explained in section 4.

240 Fig. 8 shows the induced damage contours for different fiber orientations. It can be seen that
241 the induced damage is highly dependant on the fiber orientation. In general, the damage area is
242 mainly propagated in parallel and perpendicular fibre direction as represented in Fig. 9.

243 Lower induced damages are achieved for 15° and 30° fibre orientations, while higher values are
244 obtained for 75° and 90° . The implication of high tool-workpiece contact stiffness for low fibre
245 orientations produced a fragile chip rupture without excessive damage propagation. For a fibre
246 orientation of 0° the fibre buckling effects are detected, introducing unstable effects on damage
247 propagation.

248 For higher fibre orientations the tool-workpiece contact stiffness is mainly governed by the
249 matrix; thereby it is softer than the contact produces with low fibre orientations. Due to this fact,
250 a significant energy increment is required to achieve the chip generation. As a result, the sub-
251 surface damage extension is deeper for these unidirectional composite laminates. Lastly, for a
252 fibre of 90° a fine line of the sub-surface in the thickness direction is appreciated. This finding
253 reveals a significant fibre-matrix debonding which increase the damage extension because the tool
254 pushed the fibre away.

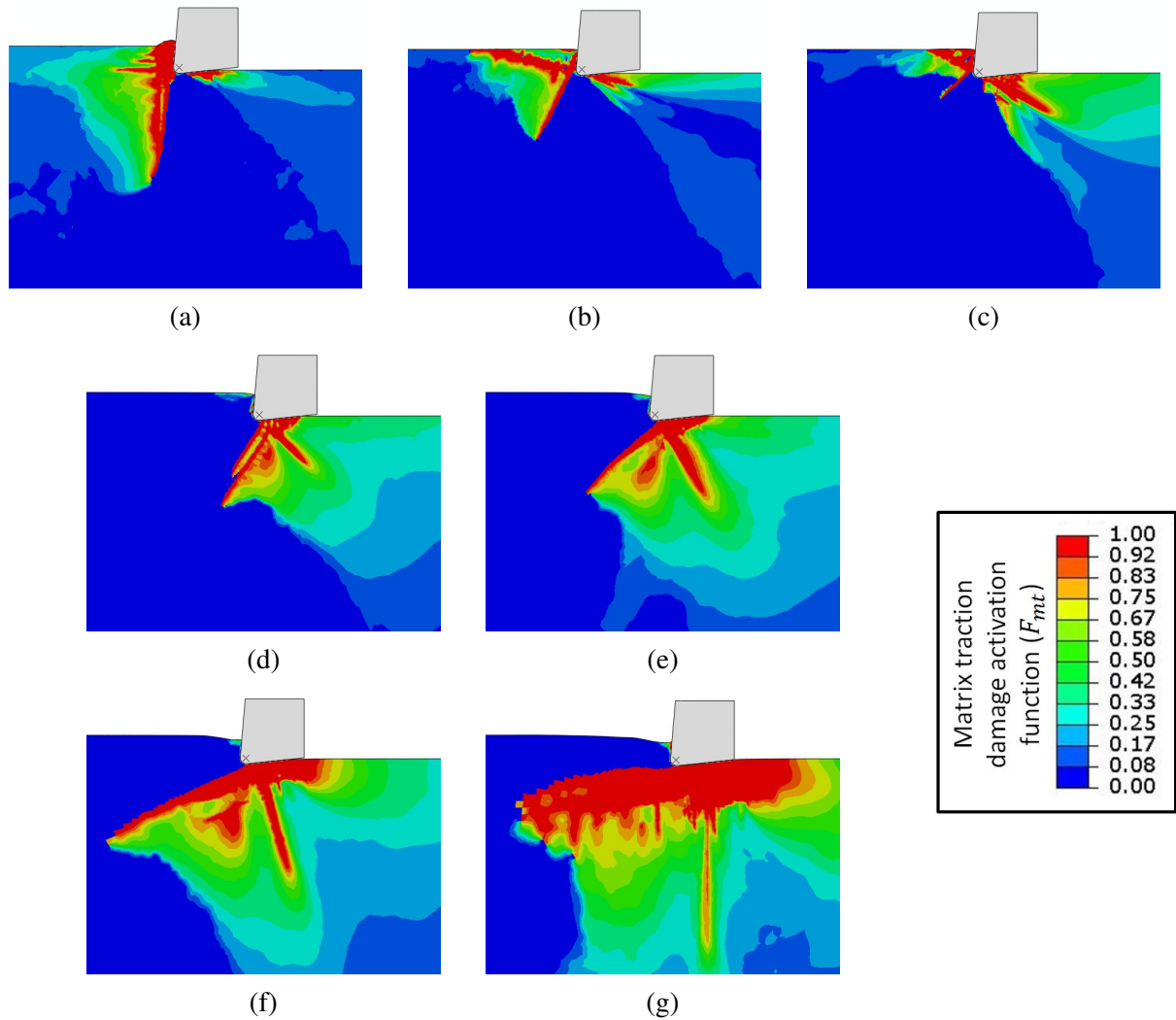


Fig. 9. F_{mt} obtained for fibre orientations (a) 0° (b) 15° , (c) 30° , (d) 45° , (e) 60° , (e) 75° and 90° at final simulation time with the standard cutting configuration.

255 5.2. Workpiece material influence

256 UD-CFRP and UD-GFRP composites are simulated to assess the influence of different material
 257 properties. It is found that levels of induced damage are significantly lower for UD-CFRP in all
 258 fibre orientations, see Fig. 11. In the case of UD-CFRP composites, a fragile damage behaviour
 259 is appreciated while UD-GFRP laminates shows a ductile behaviour. This behaviour is explained
 260 because of the higher contact stiffness properties between the tool and UD-CFRP composites.

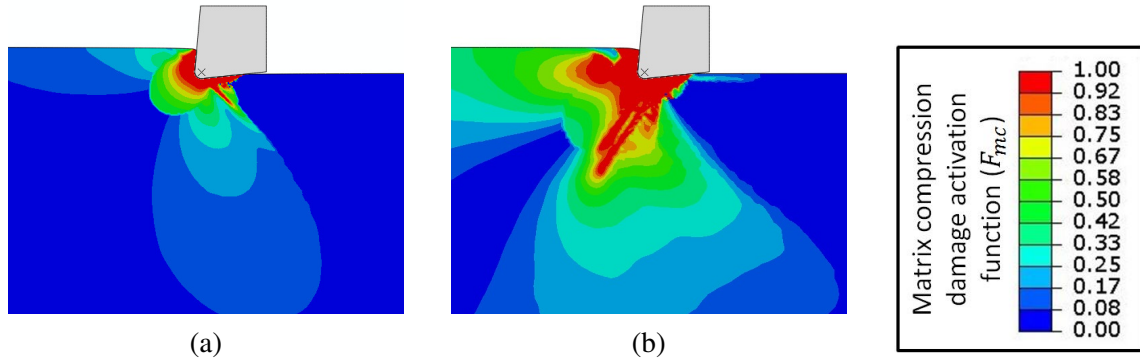


Fig. 10. F_{mc} illustration of (a) UD-CFRP composites and (b) UD-GFRP composites at final simulation time and fibre orientation of 45° .

261 The UD-GFRP composites increased more than 144.83% the machined induced damage simu-
 262 lated in UD-CFRP composites. For most fibre orientations the UD-GFRP composites sub-surface
 263 damage exceeded the 200% or even the 300% the damage obtained for UD-CFRP composites;
 264 reaching the maximum difference of a 375.76% for fibre orientation of 90° . Hence, it is concluded
 265 that CFRP composites are better materials to machine than GFRP composites in terms of induced
 266 machining damage response. An illustration of the matrix compression damage area (F_{mc}) for
 267 both materials with a fibre orientation of 45° is presented in Fig. 10.

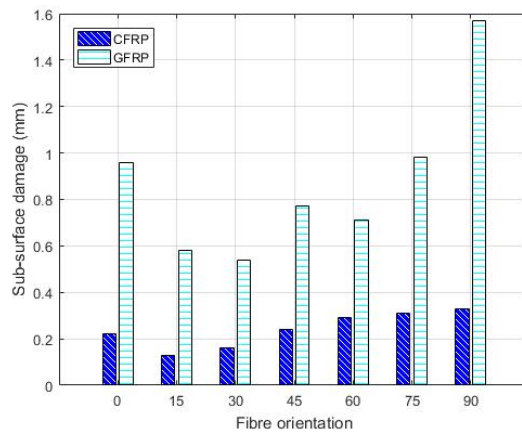


Fig. 11. Sub-surface damage obtained for all the workpiece materials and fibre orientations studied at the final simulation time.

268 Note that, because of the high stiffness of CFRP composites the machining peak forces are

269 substantially incremented in comparison with GFRP composites, as show in Fig. 12.

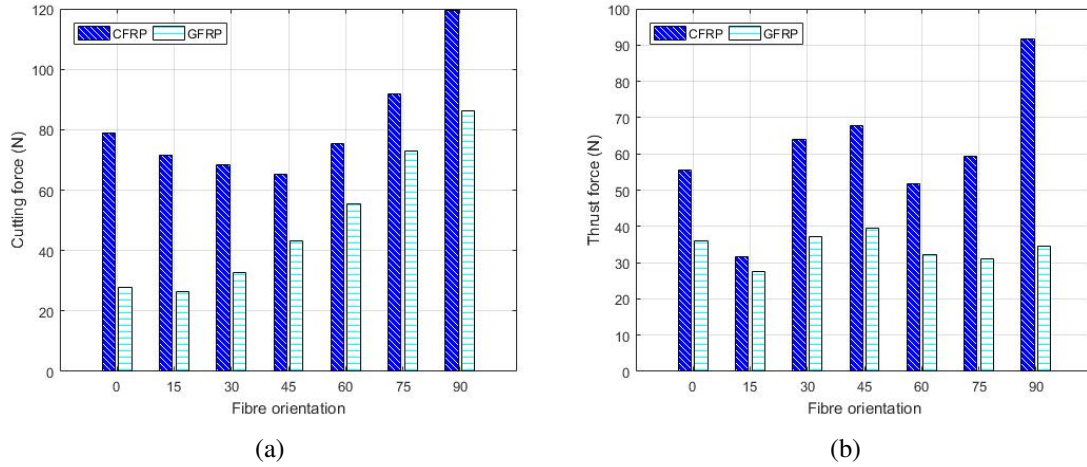


Fig. 12. (a) Cutting and (b) thrust forces obtained for all the workpiece materials and fibre orientations studied at the final simulation time.

270 *5.3. Tool edge radius influence*

271 In Fig. 13 the induced damages obtained with the 15 μm , 30 μm and 50 μm edge tool radius
 272 simulated are plotted. This increment of edge tool radius chosen is simulated to observe the effects
 273 on the laminate damage that tool wears cause. An edge radius of 15 μm represents the geometry
 274 of a new cutting tool faithfully. Whereas, radius of 30 μm and 50 μm model the increased edge
 275 radius of the cutting tools after several machining operations.

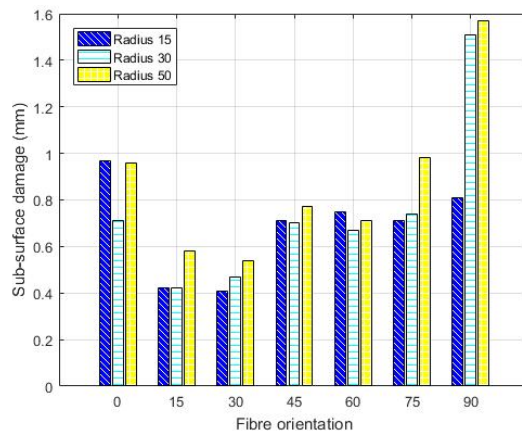


Fig. 13. Sub-surface damage obtained for all the tool edge radius and fibre orientations studied at the final simulation time.

276 For fibre orientations of 15° and 75° tool edge radius $15\mu m$ and $30\mu m$ reduce the sub-surface
 277 damage extension obtained with a tool edge radius of $50\mu m$. For 30° , 45° and 60° fibre orienta-
 278 tions, the tool edge radius influence on the subsurface damage is observed to be negligible in the
 279 studied radius range.

280 In the case of 0° , a significant damage reduction is obtained with a tool edge radius of $30\mu m$.
 281 This damage reduction is not realistic and it is reached due to the behaviour of laminates with fibre
 282 orientations of 0 degrees is especially difficult to model; in this case, fibres are parallel to the tool
 283 movement providing a rigid tool-workpiece contact making the internal damage propagation un-
 284 stable introducing significant numerical errors. For a fibre orientation of 90° , the use of a low tool
 285 edge radius is found to be highly recommended to reduce the laminate damage area significantly,
 286 see Fig. 14.

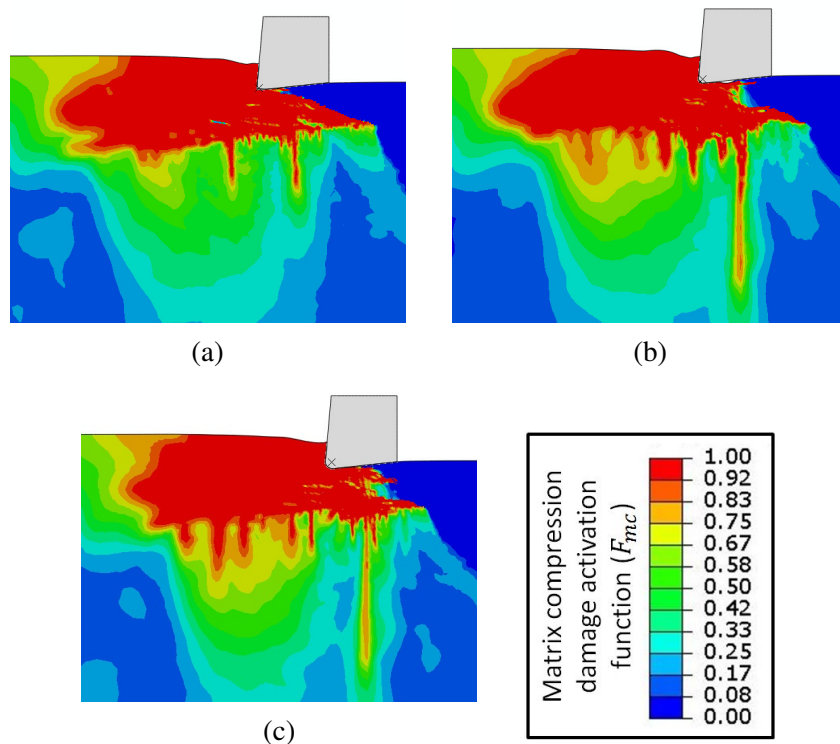


Fig. 14. F_{mc} obtained for tool edge radius of (a) $15\mu m$ (b) $30\mu m$, (c) $50\mu m$ at final simulation time for a fibre orientation of 90° .

287 It is concluded that lower tool edge radius produce better machining surfaces than cutting tools

288 with higher edges radius. However, the maximum sub-surface damage increment is observed small
 289 (below the 40%) for fibre orientations between 0° and 75° . Hence, it is determined that the tool
 290 wear until $50 \mu\text{m}$ does not increase the sub-surface damage critically for fibre orientations between
 291 0° and 75° .

292 5.4. Relief angle influence

293 Machining configurations with 4° , 6° , 8° and 10° are analysed, see Fig. 15. In general terms, the
 294 use of higher relief angles is beneficial to minimise the sub-surface damage as shown in Fig. 15(a).
 295 Same tendency is appreciated for thrust forces due to the tool-workpiece contact area reduction
 296 behind the tool tip (refer to Fig. 15(b)). Therefore, it is concluded that thrust force and induced
 297 damage are intimate related; the less thrust force is achieved, the less induced damage is obtained.

298 Relief angle 10° is found to reduce the damage for fibre orientations of 15° , 30° and 75° con-
 299 siderably. Besides, it is observed that relief angles of 8° and 10° minimised the induced damage
 300 in comparison with the rest of angles for 0° and 45° fibre orientations. For 60° fibre orientation,
 301 the relief angle effects are observed to be negligible and for 90° the relief angle of 6° a significant
 302 induce damage is achieved in comparison with the rest of angles simulated.

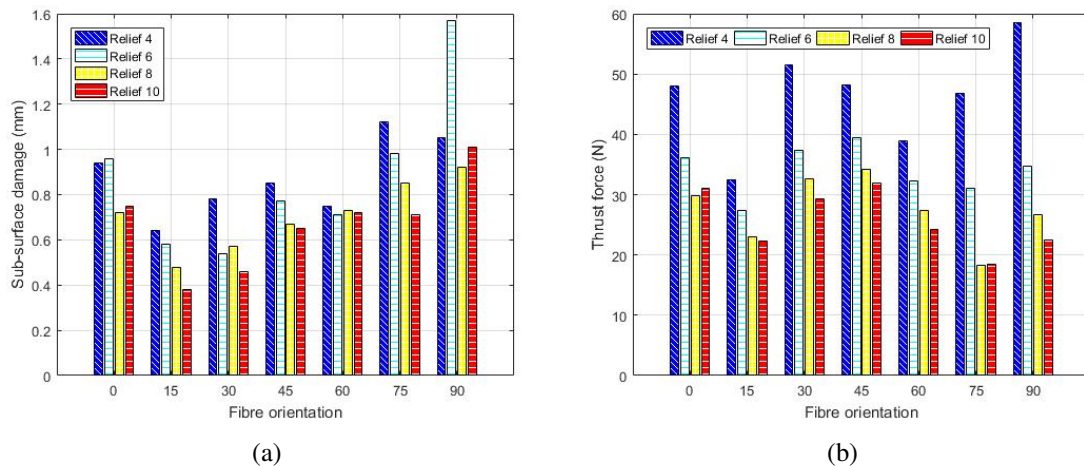


Fig. 15. (a) Sub-surface damage and (b) thrust forces obtained for all the relief angles and fibre orientations studied at the final simulation time.

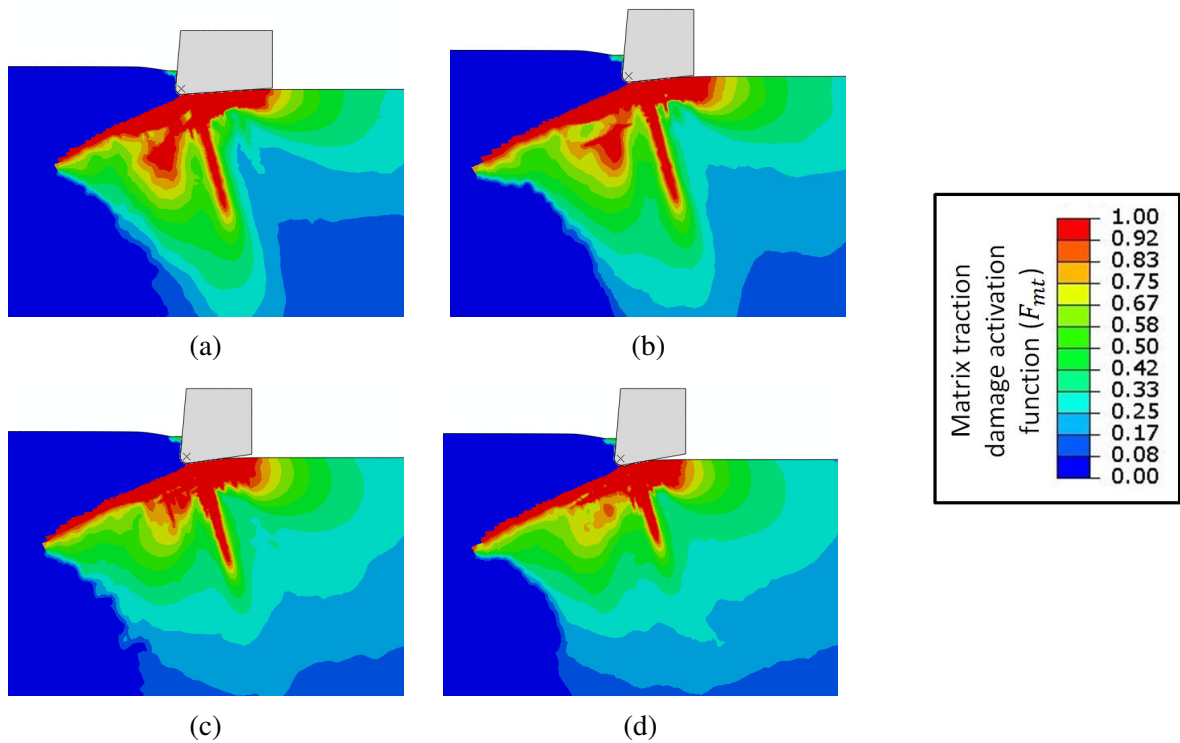


Fig. 16. F_{mt} obtained for relief angles (a) 4° (b) 6°, (c) 8° and (d) 10° at final simulation time for a fibre orientation of 75°.

303 It is appreciated that in the case of fibre orientations with 90° the results trend is not logic. For
 304 this particular case, the inclusion of an analysis of the fibre/matrix debonding could reflect better
 305 the tendency appreciated. This failure mechanism is not included in the current FE model and
 306 takes a relevant role for 90° and higher fibre orientations. The development of micro mechanical
 307 FE models with the implementation of cohesive properties between fibre and matrix are required
 308 to analyse this issue.

309 From the simulation results, it is observed that highest sub-surface damage exceeds more than
 310 50% the lowest sub-surface damage for fibre orientations of 15°, 30°, 75° and 90°. Thus, it is
 311 concluded that the election of correct high relief angles is essential for not affecting the structural
 312 integrity of the laminate considerably. The factor F_{mt} is depicted in Fig. 16 for 75° fibre orientation
 313 to show the reduction of sub-surface damage with higher relief angles.

314 5.5. Rake angle influence

315 From the numerical results obtained in this work, not a clear rake angle tendency is observed
316 to reduce the sub-surface damage. It is found that the rake angle which produced less sub-surface
317 damage is fluctuating with the fibre orientation, see Fig. 17. Therefore, the best rake angle to
318 reduce the level of damage in composite laminates should be analysed for each fibre orientation.

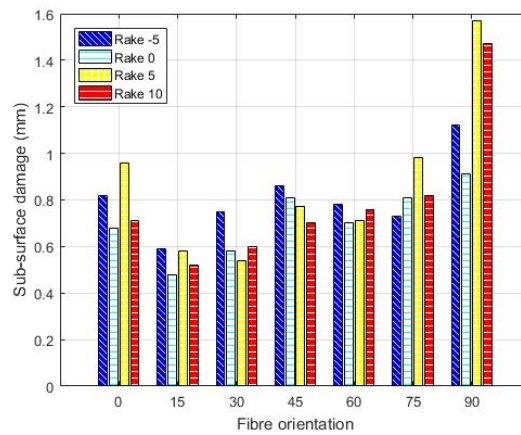


Fig. 17. Sub-surface damage obtained for all the rake angles and fibre orientations studied at the final simulation time.

319 Fig. 17 reveals that the rake angle of 0° obtains a low laminate induced damage for all fibre
320 orientations. This rake angle is found to be the best machining option for fibre orientations of 0°,
321 15°, 60° and 90°. However, significant induced damage increments is not seen for fibre orientations
322 between 0° and 75° which the maximum differences are around the 40%. Therefore, rake angle
323 is considered not essential to reduce the remaining laminate damage in comparison with other
324 cutting factors such as workpiece material or relief angle.

325 As shown in Fig. 17, rake angles of 5° and 10° are not a suitable solution for machining lam-
326 inates with 90° as it produces higher damage levels. Finally, Fig. 18 represents the matrix com-
327 pression activation function F_{mc} calculated at the final of the simulation for a fibre orientation of
328 30° as a mode of example.

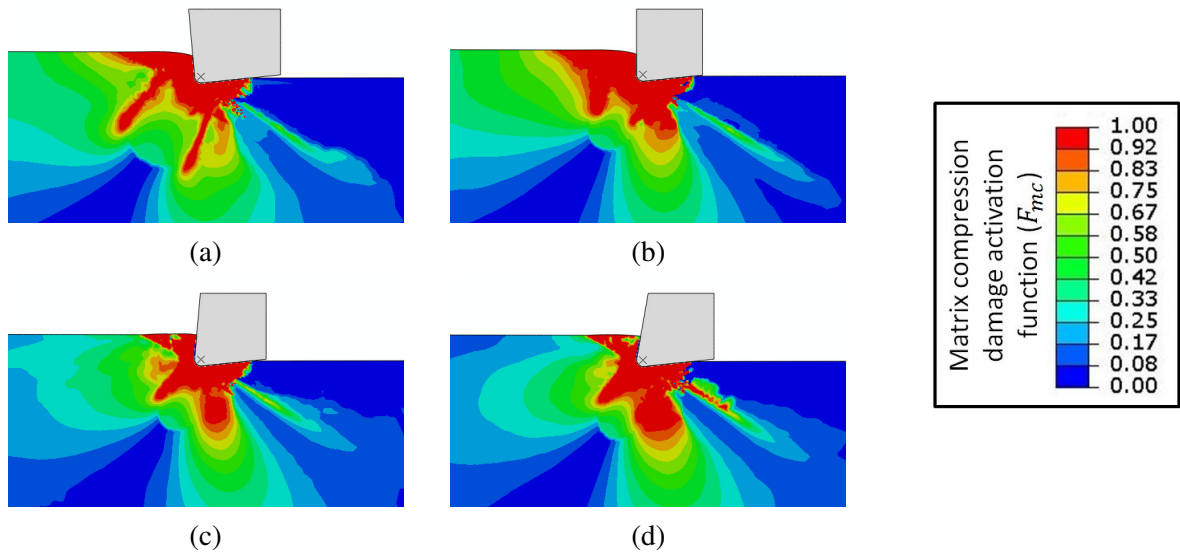


Fig. 18. F_{mc} obtained for rake angles (a) -5° (b) 0° , (c) 5° and (d) 10° at final simulation time for a fibre orientation of 30° .

329 6. Concluding remarks

330 This paper offers a novel orthogonal cutting FEM study of the effect of cutter parameters on
 331 machining induced damage. Spring back effect has been included adding a cutting tool verti-
 332 cal movement during the simulation improving the thrust force predictions. The use of a new
 333 damage algorithm composed of a linear stiffness degradation and a maximum damage limit for
 334 fibres and matrix has been demonstrated to improve previous sub-surface damage predictions. It
 335 has been demonstrated that matrix damage modes delimit the induced damage machining depth,
 336 distinguishing three main areas: (1) beneath, (2) behind and (3) in front of the cutting tool.

- 337 • Zone 1: Shear stress are predominant and as a result both matrix damages, cracking and
 338 crushing are developed.
- 339 • Zone 2: Cracking matrix mode is produced because of the tool-workpiece friction effect
 340 pull the material in this area.

341 • Zone 3: Crushing mode occurs due to the high compressive loads produce by the pushing
342 action of the cutter tool.

343 Ten cutting configurations in relation to fibre orientation, material properties, edge radius, relief
344 angle and rake angle, are simulated, concluding in the below statements.

345 • The low fibre orientations, i.e., 15° and 30°, show less induced damage than the higher
346 fibre orientations, i.e., 75° and 90°. The low fibre orientations experiencing fragile chip
347 ruptures, while higher orientations show more ductile chip rupture.

348 • The UD-CFRP composites experience more fragile chip fractures and provide much
349 lower induced damages than the UD-GFRP composites for all fibre orientations. Machin-
350 ing forces are considerably higher for CFRP composites because its superior stiffness.

351 • In general, the tool wear effects do not generate high induced damage, with the exception
352 of edge radius higher than 15 μm for 90° fibre orientation.

353 • High relief angles produce low sub-surface damages for all fibre orientations. It is noted
354 that thrust forces are intimate related to the sub-surface damage observing that the less
355 thrust force is achieved, the less induced damage is obtain.

356 • The rake angles studied does not affect considerably into the machining induced damage.
357 The use of a rake angle of 0° is recommended to obtain lower induced damage levels on
358 the laminate for every fibre orientation.

359 **Acknowledgements**

360 The first author wishes to acknowledge the financial support and technical help provided by the
361 Industrial Doctoral Centre (IDC) of Sheffield and the Engineering and Physical Sciences Research
362 Council (EPSRC) for making possible this paper.

363 The third author wishes to acknowledge the support by the Natural Science Foundation of
364 Jiangsu Province (BK20180855) and China Postdoctoral Science Foundation (2018M640459).

365 References

- 366 [1] R. M'Saoubi, D. Axinte, S. L. Soo, C. Nobel, H. Attia, G. Kappmeyer, S. Engin, and W.-M. Sim, "High perfor-
367 mance cutting of advanced aerospace alloys and composite materials," *CIRP Annals - Manufacturing Technol-*
368 *ogy*, vol. 64, no. 2, pp. 557 – 580, 2015.
- 369 [2] J. Xu, A. Mkaddem, and M. El, "Recent advances in drilling hybrid FRP / Ti composite : A state-of-the-art
370 review," *Composite Structures*, vol. 135, pp. 316–338, 2016.
- 371 [3] N. A. Abdullah, J. L. Curiel-Sosa, Z. A. Taylor, B. Tafazzolimoghaddam, J. L. Martinez Vicente, and C. Zhang,
372 "Transversal crack and delamination of laminates using XFEM," *Composite Structures*, vol. 173, pp. 78–85,
373 2017.
- 374 [4] C. Zhang, J. L. Curiel-sosa, and T. Quoc, "Meso-scale progressive damage modeling and life prediction of 3D
375 braided composites under fatigue tension loading," *Composite Structures*, vol. 201, no. June, pp. 62–71, 2018.
- 376 [5] J. L. Curiel-sosa, B. Tafazzolimoghaddam, and C. Zhang, "Modelling fracture and delamination in composite
377 laminates : Energy release rate and interface stress," *Composite Structures*, vol. 189, no. January, pp. 641–647,
378 2018.
- 379 [6] O. Nixon-Pearson and S. Hallett, "An experimental investigation into quasi-static and fatigue damage develop-
380 ment in bolted-hole specimens," *Composites Part B: Engineering*, vol. 77, pp. 462 – 473, 2015.
- 381 [7] R. Zitoune and F. Collombet, "Numerical prediction of the thrust force responsible of delamination during the
382 drilling of the long-fibre composite structures," *Composites Part A: Applied Science and Manufacturing*, vol. 38,
383 no. 3, pp. 858 – 866, 2007.
- 384 [8] C. R. Dandekar and Y. C. Shin, "Multiphase Finite Element Modeling of Machining Unidirectional Composites:
385 Prediction of Debonding and Fiber Damage," *Journal of Manufacturing Science and Engineering*, vol. 130,
386 no. 5, p. 051016, 2008.
- 387 [9] D. Nayak, N. Bhatnagar, and P. Mahajan, "Machining studies of ud-frp composites part 2: Finite element
388 analysis," *Machining Science and Technology*, vol. 9, no. 4, pp. 503–528, 2005.
- 389 [10] G. Venu Gopala Rao, P. Mahajan, and N. Bhatnagar, "Machining of UD-GFRP composites chip formation
390 mechanism," *Composites Science and Technology*, vol. 67, no. 11-12, pp. 2271–2281, 2007.
- 391 [11] K. A. Calzada, S. G. Kapoor, R. E. Devor, J. Samuel, and A. K. Srivastava, "Modeling and interpretation of fiber

- 392 orientation-based failure mechanisms in machining of carbon fiber-reinforced polymer composites,” *Journal of*
393 *Manufacturing Processes*, vol. 14, no. 2, pp. 141–149, 2012.
- 394 [12] G. V. G. Rao, P. Mahajan, and N. Bhatnagar, “Micro-mechanical modeling of machining of FRP composites -
395 Cutting force analysis,” *Composites Science and Technology*, vol. 67, no. 3-4, pp. 579–593, 2007.
- 396 [13] J. L. C. Sosa, N. Petrinic, and J. Wiegand, “A three-dimensional progressive damage model for fibre-composite
397 materials,” *Mechanics Research Communications*, vol. 35, pp. 219–221, 2008.
- 398 [14] J. L. Curiel Sosa, S. Phaneendra, and J. J. Munoz, “Modelling of mixed damage on fibre reinforced compos-
399 ite laminates subjected to low velocity impact,” *International Journal of Damage Mechanics*, vol. 22, no. 3,
400 pp. 356–374, 2013.
- 401 [15] C. G. Dávila, P. P. Camanho, and C. A. Rose, “Failure Criteria for FRP Laminates,” *Journal of Composite*
402 *Materials*, vol. 39, pp. 323–345, 2005.
- 403 [16] V. A. Phadnis, F. Makhadmeh, A. Roy, and V. V. Silberschmidt, “Drilling in carbon / epoxy composites : Experi-
404 mental investigations and finite element implementation,” *Composites Part A: Applied Science and Manufactur-*
405 *ing*, vol. 47, pp. 41–51, 2013.
- 406 [17] G. V. G. Rao, P. Mahajan, and N. Bhatnagar, “Three-dimensional macro-mechanical finite element model for ma-
407 chining of unidirectional-fiber reinforced polymer composites,” *Materials Science and Engineering A*, vol. 498,
408 no. 1-2, pp. 142–149, 2008.
- 409 [18] S. Usui, J. Wadell, and T. Marusich, “Finite element modeling of carbon fiber composite orthogonal cutting and
410 drilling,” *6th CIRP International Conference on High Performance Cutting, HPC2014*, vol. 14, pp. 211–216,
411 2014.
- 412 [19] C. Santiuste, A. Olmedo, X. Soldani, and H. Migue, “Delamination prediction in orthogonal machining of
413 carbon long fiber-reinforced polymer composites,” *Journal of Reinforced Plastics and Composites*, vol. 31 (13),
414 pp. 875–885, 2012.
- 415 [20] C. Santiuste, H. Miguélez, and X. Soldani, “Out-of-plane failure mechanisms in LFRP composite cutting,”
416 *Composite Structures*, vol. 93, no. 11, pp. 2706–2713, 2011.
- 417 [21] C. Santiuste, X. Soldani, and M. H. Miguélez, “Machining FEM model of long fiber composites for aeronautical
418 components,” *Composite Structures*, vol. 92, no. 3, pp. 691–698, 2010.
- 419 [22] S. Zenia, L. Ben Ayed, M. Nouari, and A. Delamézière, “Numerical analysis of the interaction between the
420 cutting forces, induced cutting damage, and machining parameters of CFRP composites,” *International Journal*
421 *of Advanced Manufacturing Technology*, vol. 78, no. 1-4, pp. 465–480, 2015.
- 422 [23] X. Soldani, C. Santiuste, A. Muñoz-Sánchez, and M. H. Miguélez, “Influence of tool geometry and numerical

- 423 parameters when modeling orthogonal cutting of LFRP composites,” *Composites Part A: Applied Science and*
424 *Manufacturing*, vol. 42, no. 9, pp. 1205–1216, 2011.
- 425 [24] N. Bhatnagar, D. Nayak, I. Singh, H. Chouhan, and P. Mahajan, “Determination of machining-induced damage
426 characteristics of fiber reinforced plastic composite laminates,” *Materials and Manufacturing Processes*, vol. 19,
427 no. 6, pp. 1009–1023, 2004.
- 428 [25] L. Lasri, M. Nouari, and M. El Mansori, “Modelling of chip separation in machining unidirectional FRP com-
429 posites by stiffness degradation concept,” *Composites Science and Technology*, vol. 69, no. 5, pp. 684–692,
430 2009.
- 431 [26] J. Xu and M. El Mansori, “Numerical modeling of stacked composite CFRP/Ti machining under different cutting
432 sequence strategies,” *International Journal of Precision Engineering and Manufacturing*, vol. 17, no. 1, pp. 99–
433 107, 2016.
- 434 [27] J. Xu, M. El Mansori, and J. Voisin, “Numerical Modeling and FE Analysis of CFRP/Ti Stack Orthogonal
435 Cutting,” *Procedia CIRP*, vol. 46, pp. 67–70, 2016.
- 436 [28] R. Zitoune, F. Collombet, F. Lachaud, R. Piquet, and P. Pasquet, “Experiment-calculation comparison of the cut-
437 ting conditions representative of the long fiber composite drilling phase,” *Composites Science and Technology*,
438 vol. 65, no. 3-4, pp. 455–466, 2005.
- 439 [29] C. Santiuste, J. Daz-Ivarez, X. Soldani, and H. Migulez, “Modelling thermal effects in machining of carbon fiber
440 reinforced polymer composites,” *Journal of Reinforced Plastics and Composites*, vol. 33, no. 8, pp. 758–766,
441 2014.
- 442 [30] C. R. Dandekar and Y. C. Shin, “Modeling of machining of composite materials: A review,” *International*
443 *Journal of Machine Tools and Manufacture*, vol. 57, pp. 102–121, 2012.
- 444 [31] D. Che, I. Saxena, P. Han, P. Guo, and K. F. Ehmann, “Machining of Carbon Fiber Reinforced Plastics/Polymers:
445 A Literature Review,” *Journal of Manufacturing Science and Engineering*, vol. 136, no. 3, p. 034001, 2014.
- 446 [32] N. Shetty, S. M. Shahabaz, S. S. Sharma, and S. Divakara Shetty, “A review on finite element method for
447 machining of composite materials,” *Composite Structures*, vol. 176, pp. 790–802, 2017.
- 448 [33] I. Lapczyk and J. A. Hurtado, “Progressive damage modeling in fiber-reinforced materials,” *Composites Part A:*
449 *Applied Science and Manufacturing*, vol. 38, no. 11, pp. 2333–2341, 2007.
- 450 [34] M. J. Hinton, A. S. Kaddour, and P. D. Soden, “A comparison of the predictive capabilities of current failure
451 theories for composite laminates , judged against experimental evidence,” *Composites Science and Technology*,
452 vol. 62, pp. 1725–1797, 2002.
- 453 [35] A. Puck and H. Schurmann, “Failure Analysis of Frp Laminates By Means of Physically Based Phenomenolog-

- 454 ical Models *,” *Composites Science and Technology*, vol. 3538, no. 96, pp. 1633–1662, 1998.
- 455 [36] F. Paris, J. Cañas, and J. Marin, *Introduccion al analisis y diseño con materiales compuestos*. Sevilla: Universi-
456 dad de Sevilla, Escuela Tecnica Superior de Ingenieros, 2008.
- 457 [37] C. Zhang, E. A. Duodu, and J. Gu, “Finite element modeling of damage development in cross-ply composite
458 laminates subjected to low velocity impact,” *Composite Structures*, vol. 173, no. 9, pp. 219–227, 2017.
- 459 [38] X. M. Wang and L. C. Zhang, “An experimental investigation into the orthogonal cutting of unidirectional fibre
460 reinforced plastics,” *International Journal of Machine Tools and Manufacture*, vol. 43, no. 10, pp. 1015–1022,
461 2003.